years and still lacks a general understanding [13]. Cold atom experiments find "prethermalization" to a quasi-stationary state described by a generalized Gibbs ensemble, whereas the actual thermalization appears on much longer time scales [12]. Even two distinct nonequilibrium steady states have been characterized in the Bose-Hubbard model [14], depending on the strength of the Hubbard interaction after a quench, or that a memory of the initial configuration can persist up to the largest simulation times [15].

II. THEORETICAL FRAMEWORK

A. Anharmonic chain

In this work, we consider a classical oscillator chain with an onsite anharmonic potential, as governed by the Hamiltonian

$$H = \sum_{j\in\mathbb{Z}} \left[\tfrac{1}{2}p_j^2 + \tfrac{1}{2}\omega_0^2 q_j^2 - \tfrac{1}{2}\delta\omega_0^2 (q_{j-1}q_j + q_j q_{j+1}) + \tfrac{1}{4}\lambda q_j^4 \right]. \tag{1}$$

Here ω_0^2 is the strength of the harmonic on-site interaction, $\delta\omega_0^2$ the nearest neighbor interaction, and λ the anharmonic on-site interaction, following the notations from [9]. For the numerical simulations we will use a system size L such that $j = 0, 1, \dots, L-1$ with periodic boundary conditions.

Fourier transforms are parametrized on their first Brillouin zone chosen as $\mathbb{T} = [-\frac{1}{2}, \frac{1}{2})$,

$$\widehat{f}(k) = \sum_{j\in\mathbb{Z}} \mathrm{e}^{-2\pi i k j} f_j, \quad k \in \mathbb{T}, \tag{2}$$

for which the corresponding inverse Fourier transform is

$$f_j = \int_{\mathbb{T}} \mathrm{d}k\, \mathrm{e}^{2\pi i k j} \widehat{f}(k). \tag{3}$$

For the simulations we adhere to the same convention; $j \in \mathbb{Z}$ is replaced by $j = 0, 1, \dots, L-1$ and $\mathbb{T}$ by a discrete grid with spacing $\frac{1}{L}$, i.e., $k \in \{-\frac{1}{2}, -\frac{1}{2}+\frac{1}{L}, \dots, \frac{1}{2}-\frac{1}{L}\}$.

The dispersion relation of the harmonic part obtained by setting $\lambda = 0$ above is given by [9, 11]

$$\omega(k) = \omega_0 \big(1 - 2\delta\cos(2\pi k)\big)^{1/2}. \tag{4}$$

The standard definition of the corresponding phonon mode fields $a(k)$ is then

$$a(k) = \frac{1}{\sqrt{2}} \left(\sqrt{\omega(k)}\widehat{q}(k) + i\frac{1}{\sqrt{\omega(k)}}\widehat{p}(k) \right). \tag{5}$$

With this choice, if $(q_j(t), p_j(t))$ follows the harmonic evolution, then $a(k,t)$ satisfies $\partial_t a(k,t) = -i\omega(k)a(k,t)$.

We consider here only translation invariant initial data, that is, we suppose that the initial values $(q(0), p(0))$ for the Hamiltonian evolution are chosen from some probability distribution which is invariant under periodic translations of the chain positions. This makes $q(t), p(t)$ random and the corresponding $a(k,t)$ becomes a complex-valued random field. If the initial data of the (anharmonic) evolution is translation invariant and the field has zero mean, $\langle a(k,t)\rangle = 0$, then it is possible to define the Wigner function $W_{\mathrm{mic}}(k,t)$ of the phonon field from the identity

$$\langle a(k,t)^* a(k',t)\rangle = \delta(k-k') W_{\mathrm{mic}}(k,t). \tag{6}$$

In this case, the Wigner function can thus be computed via the integral $W_{\mathrm{mic}}(k,t) = \int \mathrm{d}k' \, \langle a(k,t)^* a(k',t)\rangle$. For the finite periodic lattice used in the numerical simulations, an analogous calculation results in the definition $W_{\mathrm{mic}}(k,t) = L^{-1}\sum_{k'} \langle a(k,t)^* a(k',t)\rangle$. Since only the term with $k' = k$ yields a nonzero value in the sum, we can use the simple expression

$$W_{\mathrm{mic}}(k,t) = \frac{1}{L}\langle |a(k,t)|^2 \rangle \tag{7}$$

to compute the time evolution of the microscopic Wigner function, implicitly also depending on λ.

B. Kinetic Boltzmann–Peierls equation

A discussion about the physical and mathematical conditions and prerequisites underlying the phonon Boltzmann equation is given in [10]. Based on these ideas, the phonon Boltzmann equation for the present anharmonic chain has been derived in [9], with further details in [11].

In accordance with the microscopic model, we consider only spatially homogeneous initial data, for several reasons. First, the inhomogeneities would result in likewise spatially varying temperature distributions. Since the present systems are known to exhibit normal heat conduction [16], the temperature distribution would continue to evolve up to diffusive time scales $\mathcal{O}(L^2)$, where L is the chain length. This additional diffusive evolution complicates the study of thermalization, as it is difficult to separate the various effects. Moreover, for inhomogeneous initial data the anharmonities might lead to corrections at times $\mathcal{O}(\lambda^{-1})$, i.e., before the phonon collisions become active [17, section 6], and these corrections should first be taken into account for an honest comparison with kinetic theory.

In the homogeneous case the Wigner function depends only on the phonon wavenumber k, as defined above. The associated kinetic equation derived in [9, 11] reads

$$\partial_t W(k,t) = \mathcal{C}[W(t)](k) \tag{8}$$

with the four-phonon collision operator

$$\begin{aligned}\mathcal{C}[W](k_0) = \frac{9\pi}{4}\lambda^2 \int_{\mathbb{T}^3} \mathrm{d}k_1 \mathrm{d}k_2 \mathrm{d}k_3 \, \frac{1}{\omega_0\omega_1\omega_2\omega_3} \\ \times \delta(\omega_0+\omega_1-\omega_2-\omega_3)\delta(k_0+k_1-k_2-k_3) \\ \times \big[W_1W_2W_3 + W_0W_2W_3 - W_0W_1W_3 - W_0W_1W_2\big].\end{aligned} \tag{9}$$

Here we have used the shorthand notation $\omega_j = \omega(k_j)$ and analogously $W_j = W(k_j)$. The time t above has been scaled back to microscopic units which results in the additional factor "λ^2" compared to the formulae in [9, (3.18)].

The solutions to (8) preserve the phonon *density*,

$$\rho(t) = \int_{\mathbb{T}} \mathrm{d}k\, W(k,t) \tag{10}$$

and *energy*

$$e(t) = \int_{\mathbb{T}} \mathrm{d}k\, \omega(k) W(k,t)\,. \tag{11}$$

Let us recall that in general the phonon Boltzmann operator includes also collisions which do not preserve the phonon density $\rho(t)$: an example of such a term is obtained by swapping the sign in front of k_1 and ω_1 in the conservation delta-functions, as well as the sign of the second term inside the parentheses in (9), i.e., by changing the signs from "$++--$" to "$+---$". (The complete four-phonon collision operator for general dispersion relations is given in [9, (3.16)] and one can check that in general it conserves the energy $e(t)$ but not the density $\rho(t)$.) As proven in [10, Appendix 18.1], with more details given in [11, section 4.2.2], nearest neighbor dispersion relations do not allow for any (nontrivial) solutions to the two constraints enforced by the delta-functions in the collision operator for any three-phonon collisions, nor for any four-phonon collisions in which the positive and negative contributions do not match each other. For instance, the "$+--$" sign-combination leads to a zero contribution to the collision operator, and the remaining terms sum up to (9).

III. EQUILIBRIUM WIGNER FUNCTION

On the kinetic level, one directly verifies that

$$W^{\mathrm{eq}}_{\beta',\mu'}(k) = \frac{1}{\beta'(\omega(k)-\mu')} \tag{12}$$

are stationary solutions of (8) and (9). As shown in [10, 18], these are quite generally the only solutions for two- and higher-dimensional crystals. The one-dimensional case is more intricate but we do not expect any new solutions to appear for the nearest neighbor dispersion relations (if $\delta = \frac{1}{2}$, the proof of absence of additional solutions is given in [19, section 5]). For an arbitrary Wigner function $W(k)$, the chemical potential μ' and inverse temperature β' of the corresponding thermal equilibrium state on the kinetic level are fixed by the density and energy conservation laws.

A natural question is then whether (12) is an accurate description of a *microscopic* thermal Wigner function

$$W_\beta(k) = \frac{1}{L}\langle |a(k)|^2\rangle_\beta \tag{13}$$

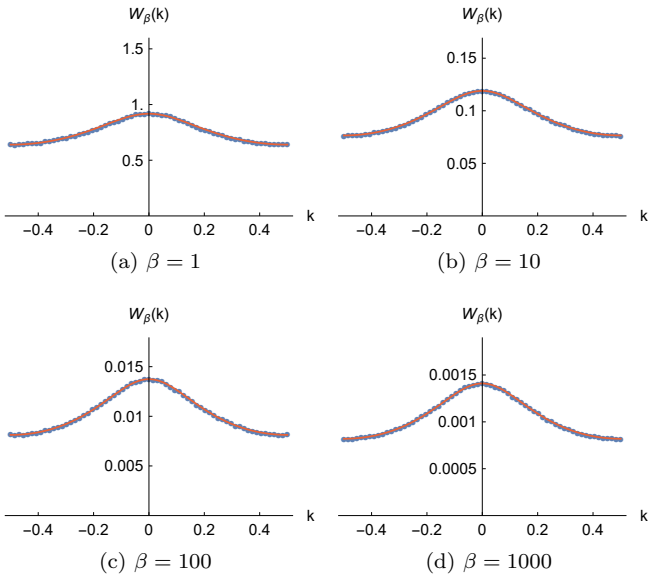

(a) $\beta = 1$ (b) $\beta = 10$ (c) $\beta = 100$ (d) $\beta = 1000$

FIG. 1. Microscopic thermal Wigner functions $W_\beta(k)$ defined in (13). The red curves show fitted kinetic equilibrium Wigner functions of the form (12).

with $a(k)$ defined in (5) and $\langle\cdot\rangle_\beta$ denoting the average with respect to the Gibbs canonical ensemble distribution

$$Z^{-1}\,\exp[-\beta H]. \tag{14}$$

To investigate this question numerically, we evaluate (13) by sampling the microscopic momenta and positions from (14). According to the Hamiltonian (1), the momenta p_j are independent Gaussian variables $\sim \exp[-\frac{1}{2}\beta p_j^2]$. The positions decouple from the momenta and are distributed as

$$Z_{\mathrm{sp}}^{-1}\,\exp[-\beta H_{\mathrm{sp}}], \tag{15}$$

with

$$H_{\mathrm{sp}} = \sum_{j=0}^{L-1}\left[\tfrac{1}{2}\omega_0^2 q_j^2 - \tfrac{1}{2}\delta\omega_0^2(q_{j-1}q_j + q_j q_{j+1}) + \tfrac{1}{4}\lambda q_j^4\right] \tag{16}$$

the spatial part of the Hamiltonian (using periodic boundary conditions). To obtain the positions in practice, we discretize the following fictitious overdamped Langevin dynamics [20] (also known as biased random-walk)

$$\mathrm{d}q_j(\tau) = -\partial_{q_j} H_{\mathrm{sp}}\,\mathrm{d}\tau + \sqrt{\tfrac{2}{\beta}}\,\mathrm{d}W_j(\tau)\,, \quad j = 0,\dots,L-1 \tag{17}$$

where $W_j(\tau)_{\tau\geq 0}$ are standard Wiener processes. Numerically, we use the Euler-Maruyama method with step size $\Delta\tau$,

$$q_j^{n+1} = q_j^n - \Delta\tau\,\partial_{q_j} H_{\mathrm{sp}} + \sqrt{\tfrac{2\Delta\tau}{\beta}}\,G_j^n\,, \tag{18}$$

where the G_j^n are independent standard Gaussian variables. In our implementation, we set $\Delta\tau = \frac{1}{64}$ and perform 1024 such steps.

The resulting $W_\beta(k)$ for four values of β is shown in Fig. 1 (blue dots). We have set $\omega_0 = 1$, $\delta = \frac{1}{4}$ and $\lambda = 1$ in the microscopic Hamiltonian, with lattice size $L = 64$. By a scaling argument [9], one finds that the anharmonic effects have a strength which depends only on λ/β. Thus for large values of β or small λ, $W_\beta(k)$ is expected to be well approximated by $W^{\mathrm{eq}}_{\beta',\mu'}(k)$ in (12). Numerical fits are shown as red curves in Fig. 1; even though λ is quite large, one observes very good agreement. The corresponding values of β' and μ' are recorded in the following table:

β	1	10	100	1000
β'	0.912	8.98	97.1	986.4
μ'	-0.488	-0.229	-0.0426	-0.0120

One observes that $\beta' \approx \beta$ and $\mu' \approx 0$ for large β.

IV. MICROSCOPIC VERSUS KINETIC DYNAMICS AND THERMALIZATION

First, we explore at which time scales and with which accuracy the kinetic description is a good approximation to the microscopic dynamics. For that purpose, we compute the time dependent $W_{\mathrm{mic}}(k,t)$ as defined in Eq. (7) from the microscopic field variables, averaging over many realizations of the microscopic dynamics. This "microscopic" Wigner function is then compared to the solution of the kinetic Boltzmann equation in (8).

Specifically, we choose the chain length $L = 64$ and Hamiltonian parameters $\omega_0 = 1$, $\delta = 1/4$, $\lambda = 1$ or $\lambda = \frac{1}{2}$. For the numerical time evolution we use the symplectic Störmer-Verlet method [21] with step size $\Delta t = 0.001$. $W_{\mathrm{mic}}(k,t)$ is averaged over 10^5 realizations of the microscopic dynamics.

A. Bimodal momentum distribution

Concerning initial states, we sample the initial momenta p_j, $j = 0, 1, \ldots, L-1$ independently from the bimodal distribution

$$Z_{\mathrm{init}}^{-1} \exp\left[-\beta_{\mathrm{init}}\left(4p_j^4 - \tfrac{1}{2}p_j^2\right)\right] \tag{19}$$

with $\beta_{\mathrm{init}} = 1000$, which by construction markedly differs from the thermodynamic Gaussian equilibrium distribution. On the other hand, the initial positions are sampled from the thermodynamic Gibbs ensemble (15) with $\beta = \beta_{\mathrm{init}}$. These initial distributions satisfy an important prerequisite for the theoretical derivation of the kinetic Boltzmann equation, namely translational invariance. We set $\lambda = 1$ in what follows.

As preliminary characterization of the microscopic dynamics, we compute histograms of the momenta $p_j(t)$ to obtain the time evolution of the momentum distribution. It is shown as blue curve in Fig. 2 for several time points. The red dashed curve at $t = 0$ is the initial distribution (19), which – by construction – precisely matches the numerical distribution. One observes that the momentum distribution relaxes very quickly to a Gaussian-shaped curve already at $t = 16$. Nevertheless, it keeps slightly oscillating until finally settling towards a Gaussian dis-

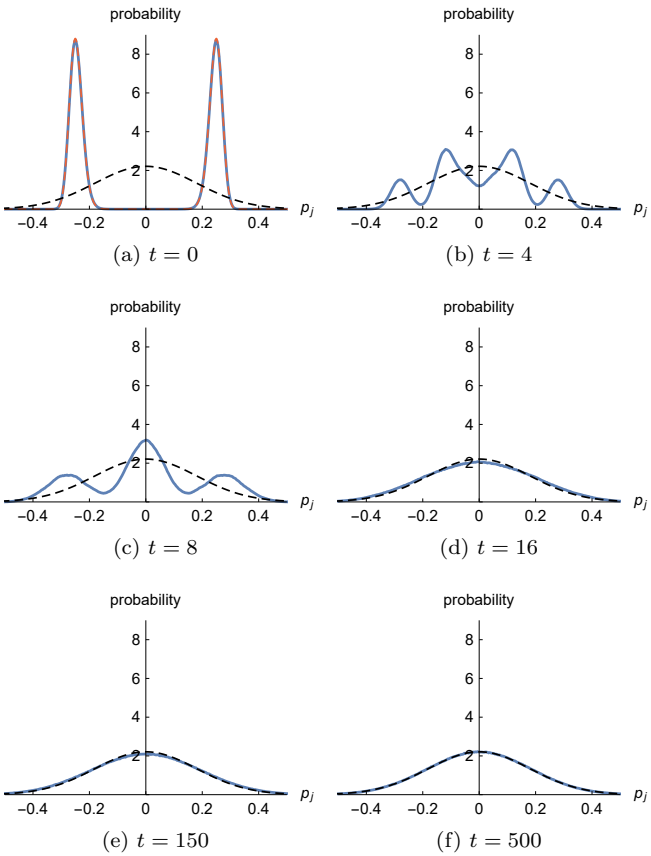

FIG. 2. Time evolution of the momentum distribution (blue curve), based on the microscopic dynamics and initialized via (19) (red dashed) at $t = 0$.

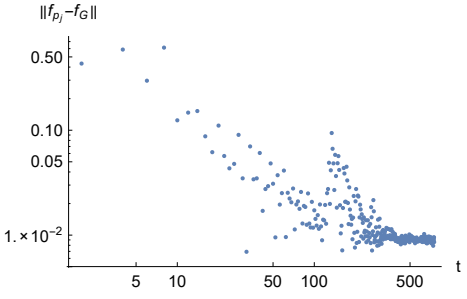

FIG. 3. Convergence of the momentum distribution shown in Fig. 2 towards the stationary Gaussian distribution (20).

tribution

$$\frac{1}{\sqrt{2\pi/\beta_{\rm th}}}\exp\left[-\tfrac{1}{2}\beta_{\rm th}\,p^2\right] \tag{20}$$

with fitted $\beta_{\rm th} = 30.74$, shown as black dashed curve in Fig. 2. The L^2-norm distance to this Gaussian distribution is quantified in Fig. 3. Following the initial exponential convergence up to around $t = 50$, one observes a temporary increase of the distance between $t = 100$ and $t = 200$, corresponding to the mentioned slight oscillations. At around $t = 500$ the momentum distribution has reached stationarity.

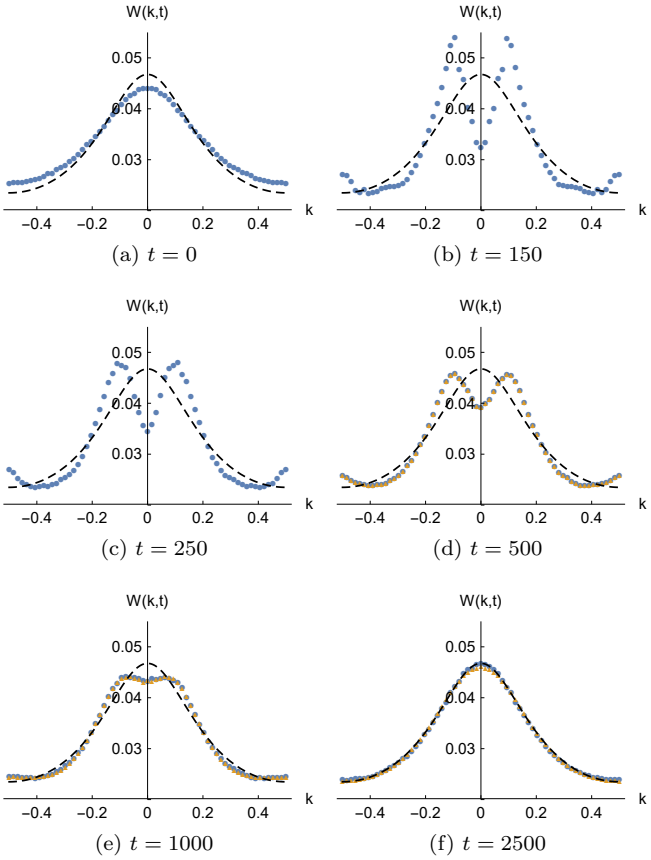

(a) $t = 0$ (b) $t = 150$ (c) $t = 250$ (d) $t = 500$ (e) $t = 1000$ (f) $t = 2500$

FIG. 4. Time evolution of the Wigner function computed from microscopic field variables (blue dots), in comparison with a simulation of the kinetic Boltzmann equation (yellow triangles) starting at $t = 500$.

Based on the microscopic field variables, we now compute the time evolution of the Wigner function via (7), which is shown as blue dots in Fig. 4. Around $t = 150$ (in the oscillatory regime of the momentum distribution), it exhibits a somewhat "excited" form. Surprisingly, at $t = 500$ when the momentum distribution has already reached stationarity, the Wigner function clearly differs from an equilibrium shape as discussed in Sec. III. On the other hand, from around $t = 500$ one observes that the microscopic Wigner function starts a smooth transition towards the black dashed curve $1/(\beta'(\omega(k)-\mu'))$ in Fig. 4 with fitted $\beta' = 40.91$ and $\mu' = 0.1842$. One is drawn to hypothesize that the kinetic description is applicable in this regime. To quantify, we numerically solve the kinetic Boltzmann equation (8) starting at $t = 500$, with the initial kinetic Wigner function set equal to the microscopic Wigner function at $t = 500$. For the kinetic collision operator we adapt the numerical procedure described in [22] to the present setting. The kinetic solution is sped up by a factor 4/3 to align it with the microscopic time evolution, and shown superimposed as yellow triangles in Fig. 4. The microscopic and kinetic Wigner functions agree fairly well. The required 4/3 time scaling factor could stem from the relatively large anharmonic coefficient $\lambda = 1$; namely, the theoretical derivation of the kinetic Boltzmann equation uses an expansion for small λ. To check, we have repeated the simulation with the same parameters except $\lambda = \frac{1}{2}$, with qualitatively very similar results (data not shown). Besides the theoretical time scale $\lambda^{-2}t$, the correction speed up factor is now approximately 1/0.85, i.e., closer to 1 than for $\lambda = 1$.

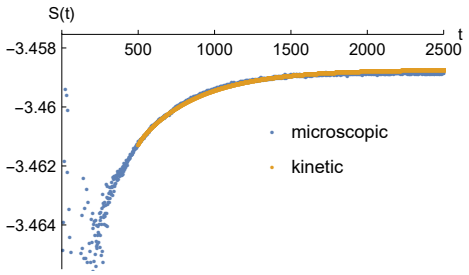

FIG. 5. Time evolution of the entropy computed via (21), superimposing the microscopic with the kinetic simulation.

The entropy based on the phonon Wigner function is defined as

$$S(t) = \int_{\mathbb{T}} {\rm d}k\, \log W(k,t). \tag{21}$$

On the kinetic level, the H-theorem states that the entropy is monotonically increasing with time. Fig. 5 compares the entropy computed from the microscopic Wigner function with the entropy based on the Wigner function on the kinetic level, starting at $t = 500$ and using the

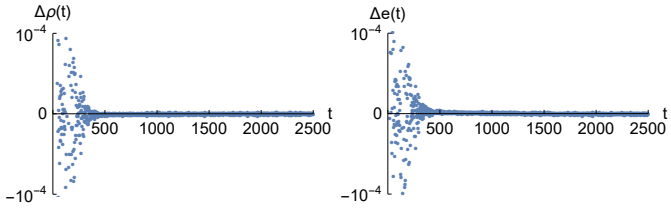

(a) $\rho_{\rm mic}(t) - \rho_{\rm mic}(t_{\rm max})$ (b) $e_{\rm mic}(t) - e_{\rm mic}(t_{\rm max})$

FIG. 6. Time evolution of the density and energy difference computed via (10) and (11) from the microscopic Wigner function shown in Fig. 4.

same 4/3 time scaling factor as before. As expected from Fig. 4, the agreement is fairly good, and the entropy is indeed monotonically increasing.

Finally, Fig. 6 shows the time evolution of the density and energy computed via (10) and (11) from the microscopic Wigner function, after subtracting the final density and energy, respectively. Their numerical values are $\rho_{\rm mic}(t_{\rm max}) = 0.0324$ and $e_{\rm mic}(t_{\rm max}) = 0.0304$. One can discriminate an initial time interval up to $t \approx 500$ where the density and energy are not exactly preserved. After that, density and energy conservation holds quite precisely, in accordance with the kinetic Boltzmann equation. Nevertheless, the density conservation is surprising since the Wigner function is computed from the microscopic fields, but on the microscopic level only the energy is expected to be conserved.

B. Random phase approximation for the initial Wigner function

In the previous subsection we have specified the microscopic Wigner function at $t = 0$ only indirectly via the position and momentum distributions. An alternative route to start from an arbitrary prescribed Wigner function $W_0(k)$ consists of "inverting" Eq. (7) and setting

$$a(k) = \sqrt{L\, W_0(k)}\, \mathrm{e}^{i\varphi(k)}, \tag{22}$$

with uniformly distributed random variables $\varphi(k) \in [0, 2\pi]$, independently for each discretized k. One can check that all odd moments of the field a are then initially zero, since $\langle \mathrm{e}^{i\varphi(k)} \rangle = 0$, $\langle \mathrm{e}^{i(\varphi(k)+\varphi(k'))} \rangle = 0$, etc. It straightforwardly follows that the odd moments are zero for all times t, and we find in particular that $\langle a(k,t) \rangle = 0$. By these properties the initial, hence also time-evolved, field is translation invariant: lattice translation by x_0 corresponds to multiplication of $a(k)$ by a factor $\mathrm{e}^{2\pi i k x_0}$, i.e., a nonrandom phase. As $\varphi(k)$ is uniformly distributed on $[0, 2\pi]$, the random variables $\mathrm{e}^{i\varphi(k)}$ and $\mathrm{e}^{i(\varphi(k)+2\pi k x_0)}$ have the same distribution for all k, x_0.

In the numerical simulation we set

$$W_0(k) = \tfrac{1}{40}\Big(\sin(2\pi k)^2 + \mathrm{e}^{\sin(\pi(k-1/3))^2 - 1} + \tfrac{1}{4}\cos(8\pi k) \Big). \tag{23}$$

For each realization of $a(k)$, the initial microscopic positions and momenta are determined by inverting Eq. (5). We then solve the microscopic time evolution as before, with parameters $L = 64$, $\omega_0 = 1$, $\delta = 1/4$ and $\lambda = \frac{1}{2}$. The time dependent momentum and position distribution and microscopic Wigner function is averaged over 10^5 such realizations.

Different from the previous simulation example, one now observes that the momentum and position distributions remain constant in time, as shown in Fig. 7 with three time points superimposed. Analogous to the previous analysis, the black dashed line in the left subfigure is a Gaussian distribution (20) with fitted $\beta_{\rm th} = 35.00$.

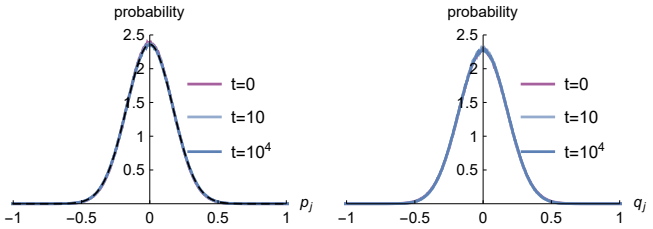

FIG. 7. Momentum and position distributions based on the microscopic dynamics with initial "random phase" field (22), staying constant in time. The black dashed line on the left is a Gaussian distribution (20) with fitted $\beta_{\rm th} = 35.00$.

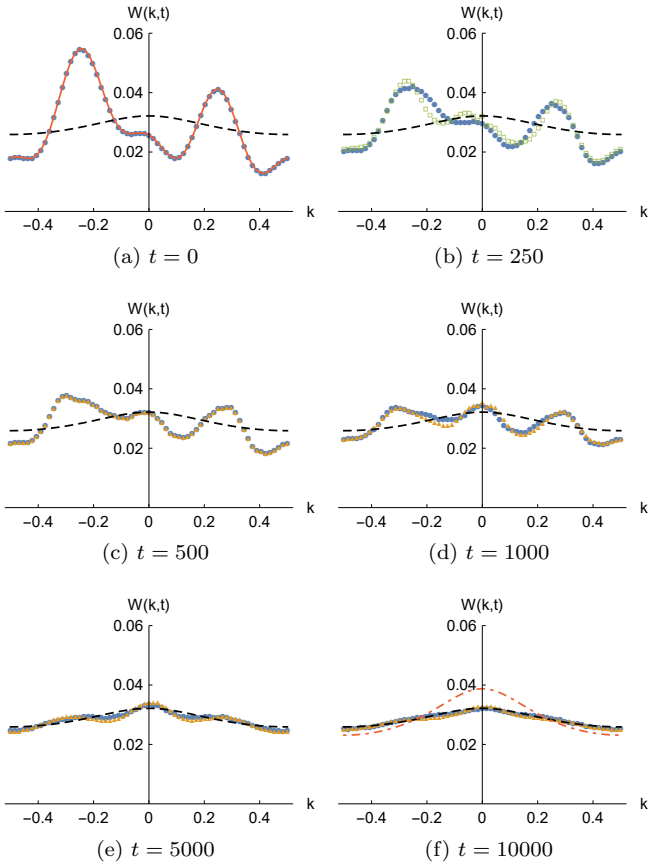

(a) $t = 0$ (b) $t = 250$ (c) $t = 500$ (d) $t = 1000$ (e) $t = 5000$ (f) $t = 10000$

FIG. 8. Time evolution of the Wigner function computed from microscopic field variables (blue dots) with initial "random phase" field (22), in comparison with the kinetic Boltzmann solution (yellow triangles) starting at $t = 500$.

The time evolution of the microscopic Wigner function is visualized as blue dots in Fig. 8. The faint red curve at $t = 0$ shows the analytic form in (23). Note that the equilibration time is now longer, as expected from the theoretical $\lambda^{-2}t$ time scale with $\lambda = \frac{1}{2}$ instead of $\lambda = 1$. As before, there seems to be an initial transient time period which is not well described by the kinetic Boltzmann equation. This is noticeable when comparing the microscopic Wigner function with the kinetic solution

starting at $t = 0$, shown as superimposed green squares at $t = 250$ in Fig. 8b. For the present simulation, the extent of this transient period is not discernible from the momentum distribution, and currently we are not aware of a good indicator. Nevertheless, one expects that the kinetic Boltzmann description becomes applicable after this transient period. As test, we compare the microscopic Wigner function with the kinetic solution starting at $t = 500$, shown as yellow triangles in Fig. 8. The time evolution is adjusted by the theoretical $\lambda^{-2}t$ scale, without any further correction factor. The agreement is reasonably good, but not as precise as the simulation results in Fig. 4. The deviation could stem from the fact that the transient period extends beyond $t = 500$, or the still relatively large $\lambda = \frac{1}{2}$ compared to the theoretical perturbation expansion for small λ.

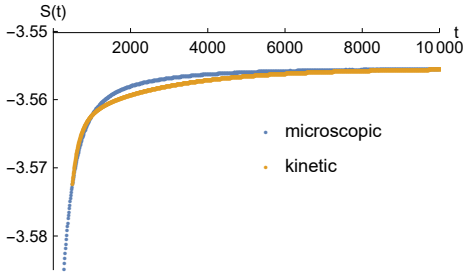

FIG. 9. Time evolution of the entropy based on the Wigner functions in Fig. 8, superimposing the microscopic "random phase" simulation with the kinetic solution starting at $t = 500$.

Fig. 9 shows a comparison of the microscopic and kinetic entropies. As expected from Fig. 8, the agreement is less precise than in Fig. 5; nevertheless, the values at the largest time are very close, and the entropies are monotonically increasing, in accordance with the H-theorem.

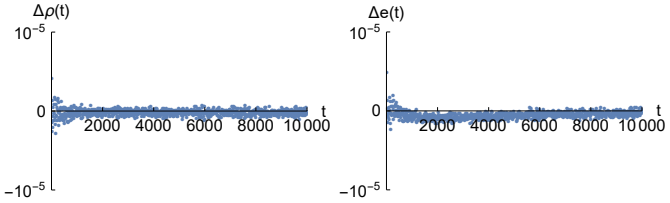

(a) $\rho_{\rm mic}(t) - \rho_{\rm mic}(t_{\rm max})$ (b) $e_{\rm mic}(t) - e_{\rm mic}(t_{\rm max})$

FIG. 10. Time evolution of the density and energy difference based on the microscopic Wigner function shown in Fig. 8.

The time evolution of the density and energy based on the microscopic Wigner function is visualized in Fig. 10, after subtracting the density $\rho_{\rm mic}(t_{\rm max}) = 0.0287$ and energy $e_{\rm mic}(t_{\rm max}) = 0.0278$ at the largest simulation time $t_{\rm max} = 10000$, respectively. One observes that both are conserved very well during the time evolution, with deviations on the order of 10^{-6}, which are presumably due to statistical noise. We use the density and energy at $t_{\rm max}$ to compute the kinetic equilibrium Wigner function of the form $1/(\beta'(\omega(k) - \mu'))$, see Eq. (12). That is, we fit β' and μ' numerically such that $1/(\beta'(\omega(k) - \mu'))$ has density $\rho_{\rm mic}(t_{\rm max})$ and energy $e_{\rm mic}(t_{\rm max})$, obtaining $\beta' = 14.50$ and $\mu' = -1.438$. The result is shown as black dashed curve in Fig. 8, which fits the microscopic Wigner function at the largest simulation time very well.

On the other hand, we have seen in Fig. 7a that the "microscopic" inverse temperature equals $\beta_{\rm th} = 35$. Repeating the computations in Sec. III for $\beta_{\rm th}$, one obtains the microscopic thermal Wigner function $W_{\beta_{\rm th}}(k)$ shown as dot-dashed red curve in Fig. 8f. Surprisingly, $W_{\beta_{\rm th}}(k)$ clearly deviates from the microscopic Wigner function at $t_{\rm max}$. Our interpretation is that the microscopic Wigner function has not reached its asymptotic $t \to \infty$ form, but is constrained by the quasi-conserved density shown in Fig. 10a. The Wigner function should eventually converge to $W_{\beta_{\rm th}}(k)$ for much longer simulation times, since only the energy is conserved on the microscopic level. As an appreciation of the long time scales, the entropy of $W_{\beta_{\rm th}}(k)$ equals -3.54275, which is noticeably larger than the entropies shown in Fig. 9.

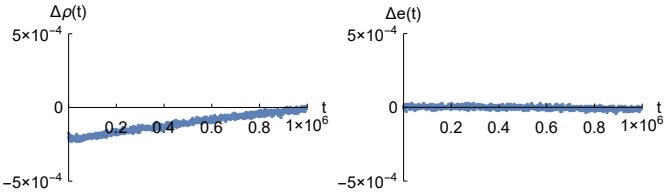

(a) $\rho_{\rm mic}(t) - \rho_{\rm mic}(t_{\rm max})$ (b) $e_{\rm mic}(t) - e_{\rm mic}(t_{\rm max})$

FIG. 11. Time evolution of the density and energy difference using the same simulation parameters as in Fig. 10, except for larger $\lambda = 10$ and longer simulation time $t_{\rm max} = 10^6$. Note the different scale of the y-axis compared to Fig. 10.

To check the long-time convergence hypothesis, we have repeated the simulation with the same initial Wigner function and simulation parameters, except for larger $\lambda = 10$ to increase the anharmonic effects, and longer simulation time $t_{\rm max} = 10^6$. Fig. 11 shows the time evolution of the density and energy analogous to Fig. 10. Indeed one observes a drift of the density, while the energy remains constant (up to statistical noise). Due to the increased computational effort associated with $t_{\rm max} = 10^6$, averages are taken with respect to 10^4 realizations instead of 10^5. Even at $t_{\rm max}$, the microscopic Wigner function still deviates from the microscopic thermal Wigner function (data not shown), but the drift of the density and conservation of the energy supports the expected convergence at even longer time scales.

V. CONCLUSIONS

The kinetic Boltzmann–Peierls description cannot account for the eventual density relaxation, but nevertheless explains one time scale of the equilibration pro-

cess. Moreover, it is quite insensitive to the anharmonic strength λ: in our simulations with relatively large $\lambda = \frac{1}{2}$ and $\lambda = 1$, good agreement between the microscopic and kinetic Wigner functions is found, even for much longer than suggested by the $\mathcal{O}(\lambda^{-2})$ kinetic scaling limit. While this can be partially explained by the small values of the initial fields, i.e., by focusing on low temperatures which subdue the anharmonic effects, the agreement for large λ is still surprising.

A natural follow-up question is whether kinetic descriptions can be likewise utilized for understanding thermalization of quantum systems, and whether such descriptions are applicable beyond weak interactions. While the microscopic simulation of interacting quantum systems is usually much more demanding [23] than classical molecular dynamics simulations, there is little difference in solving their respective kinetic limits, the quantum Boltzmann–Nordheim and Boltzmann–Peierls equations. The former traces back to Nordheim in 1928 [24] and is also referred to as Uehling-Uhlenbeck equation [25]. A derivation without spin can be found in [26], and an analogous derivation and simulation for the standard fermionic Hubbard-model with spin is provided in [27–29]. Similar kinetic descriptions have indeed already been used to study thermalization in the Hubbard model [30, 31], but much is still left as future work.

Acknowledgments. We would like to thank Herbert Spohn for many helpful discussions. C. B. Mendl acknowledges the hospitality of Duke university during a research visit, and support from the Humboldt foundation via a Feodor Lynen fellowship. The work of J. Lu is supported in part by the National Science Foundation under grant DMS-1454939. J. Lukkarinen has been supported by the Academy of Finland via the Centre of Excellence in Analysis and Dynamics Research (project 271983) and from an Academy Project (project 258302). The numerical simulations for this work used computational resources of the Leibniz-Rechenzentrum, München.

[1] E. Fermi, J. Pasta, and S. Ulam. Studies in nonlinear problems, I. In A. C. Newell, editor, *Nonlinear Wave Motion*, pages 143–156. American Mathematical Society, 1974. Orignally published as Los Alamos Report LA-1940 in 1955.

[2] M. Pettini, L. Casetti, M. Cerruti-Sola, R. Franzosi, and E. G. D. Cohen. Weak and strong chaos in Fermi-Pasta-Ulam models and beyond. *Chaos*, 15:015106, 2005.

[3] N. J. Zabusky and M. D. Kruskal. Interaction of "solitons" in a collisionless plasma and the recurrence of initial states. *Phys. Rev. Lett.*, 15:240–243, 1965.

[4] G. Benettin and A. Ponno. Time-scales to equipartition in the Fermi-Pasta-Ulam problem: Finite-size effects and thermodynamic limit. *J. Stat. Phys.*, 144:793–812, 2011.

[5] R. Peierls. Zur kinetischen Theorie der Wärmeleitung in Kristallen. *Ann. Phys.*, 395:1055–1101, 1929.

[6] N. Mingo and D. A. Broido. Length dependence of carbon nanotube thermal conductivity and the "problem of long waves". *Nano Lett.*, 5:1221–1225, 2005.

[7] D. Donadio and G. Galli. Thermal conductivity of isolated and interacting carbon nanotubes: Comparing results from molecular dynamics and the Boltzmann transport equation. *Phys. Rev. Lett.*, 99:255502, 2007. Erratum: 103:149901, 2009.

[8] A. J. H. McGaughey and M. Kaviany. Quantitative validation of the Boltzmann transport equation phonon thermal conductivity model under the single-mode relaxation time approximation. *Phys. Rev. B*, 69:094303, 2004. Erratum, 79:189901, 2009.

[9] K. Aoki, J. Lukkarinen, and H. Spohn. Energy transport in weakly anharmonic chains. *J. Stat. Phys.*, 124:1105–1129, 2006.

[10] H. Spohn. The phonon Boltzmann equation, properties and link to weakly anharmonic lattice dynamics. *J. Stat. Phys.*, 124:1041–1104, 2006. Erratum, 123:707, 2006.

[11] J. Lukkarinen. Kinetic theory of phonons in weakly anharmonic particle chains. In S. Lepri, editor, *Thermal Transport in Low Dimensions: From Statistical Physics to Nanoscale Heat Transfer*, volume 921 of *Lecture Notes in Physics*, chapter 4, pages 159–214. Springer, 2016.

[12] M. Gring, M. Kuhnert, T. Langen, T. Kitagawa, B. Rauer, M. Schreitl, I. Mazets, D. Adu Smith, E. Demler, and J. Schmiedmayer. Relaxation and prethermalization in an isolated quantum system. *Science*, 337:1318–1322, 2012.

[13] A. Polkovnikov, K. Sengupta, A. Silva, and M. Vengalattore. Colloquium: Nonequilibrium dynamics of closed interacting quantum systems. *Rev. Mod. Phys.*, 83:863–883, 2011.

[14] C. Kollath, A. M. Läuchli, and E. Altman. Quench dynamics and nonequilibrium phase diagram of the Bose-Hubbard model. *Phys. Rev. Lett.*, 98:180601, 2007.

[15] M. C. Bañuls, J. I. Cirac, and M. B. Hastings. Strong and weak thermalization of infinite nonintegrable quantum systems. *Phys. Rev. Lett.*, 106:050405, 2011.

[16] S. Lepri, R. Livi, and A. Politi. Thermal conduction in classical low-dimensional lattices. *Phys. Rep.*, 377:1–80, 2003.

[17] J. Lukkarinen and M. Marcozzi. Wick polynomials and time-evolution of cumulants. *J. Math. Phys.*, 57:083301, 2016.

[18] H. Spohn. Collisional invariants for the phonon Boltzmann equation. *J. Stat. Phys.*, 124:1131–1135, 2006.

[19] J. Lukkarinen and H. Spohn. Anomalous energy transport in the FPU-β chain. *Comm. Pure Appl. Math.*, 61:1753–1786, 2008.

[20] B. Leimkuhler and C. Matthews. *Molecular Dynamics - With Deterministic and Stochastic Numerical Methods*, volume 39 of *Interdisciplinary Applied Mathematics*. Springer, 2015.

[21] E. Hairer, C. Lubich, and G. Wanner. *Geometric Numerical Integration*. Springer, 2006.

[22] M. L. R. Fürst, C. B. Mendl, and H. Spohn. Matrix-valued Boltzmann equation for the non-integrable Hubbard chain. *Phys. Rev. E*, 88:012108, 2013.

[23] R. M. Martin, L. Reining, and D. M. Ceperley. *Interacting Electrons: Theory and Computational Approaches*. Cambridge University Press, 2016.

[24] L. W. Nordheim. On the kinetic method in the new statistics and its application in the electron theory of conductivity. *Proc. R. Soc.*, 119:689–698, 1928.

[25] E. A. Uehling and G. E. Uhlenbeck. Transport phenomena in Einstein-Bose and Fermi-Dirac gases. I. *Phys. Rev.*, 43:552–561, 1933.

[26] J. Lukkarinen and H. Spohn. Not to normal order – Notes on the kinetic limit for weakly interacting quantum fluids. *J. Stat. Phys.*, 134:1133–1172, 2009.

[27] M. L. R. Fürst, J. Lukkarinen, H. Spohn, and P. Mei. Derivation of a matrix-valued Boltzmann equation for the Hubbard model. *J. Phys. A: Math. Theor.*, 46:485002, 2013.

[28] J. Lukkarinen, P. Mei, and H. Spohn. Global well-posedness of the spatially homogeneous Hubbard-Boltzmann equation. *Comm. Pure Appl. Math.*, 68:758–807, 2015.

[29] M. L. R. Fürst, C. B. Mendl, and H. Spohn. Matrix-valued Boltzmann equation for the Hubbard chain. *Phys. Rev. E*, 86:031122, 2012.

[30] M. Moeckel and S. Kehrein. Interaction quench in the Hubbard model. *Phys. Rev. Lett.*, 100:175702, 2008.

[31] M. Stark and M. Kollar. Kinetic description of thermalization dynamics in weakly interacting quantum systems. *arXiv:1308.1610*, 2013.